

### **3.2.2 Fischer-Tropsch Synthesis. Electron Microdiffraction Study of Ultrafine Iron**

#### **Oxide Catalysts**

##### **ABSTRACT**

An ultrafine (3.0  $\mu\text{m}$ , 300  $\text{m}^2/\text{g}$ ) iron oxide sample has been activated in carbon monoxide and then utilized for the conversion of syngas ( $\text{H}_2/\text{CO} = 0.7$ ) at 270°C and 170 psig (1.17 MPa). The sample, after activation for 24 hrs. in CO and exposure for 2 hrs. to syngas, was shown from TEM microdiffraction data to be composed primarily of iron carbides (mainly  $\text{Fe}_3\text{C}$ ). As exposure to syngas continued, carbide particles were converted to  $\text{Fe}_3\text{O}_4$  and  $\text{Fe}_{2.2}\text{C}$  phases. The iron oxide and iron carbide phases appear to have a similar particle size distribution. The TEM data for identification of iron phases (carbide and oxide) agree with earlier Mössbauer characterization data.

##### **INTRODUCTION**

Iron-based catalysts are widely utilized for the Fischer-Tropsch Synthesis (FTS) (1). It has unique properties compared to other potential catalysts; these include activity for the water-gas-shift reaction and the potential to form a stable carbide under synthesis conditions (2). During activation and synthesis, the gas composition in contact with the catalyst has the potential to exhibit either reducing or oxidizing properties. Thus, a variety of iron oxide/carbide phases may be encountered during the activation/synthesis process.

For example, starting with metallic iron, formed by the reduction of an oxide precursor, a mixture of  $\alpha\text{-Fe}$ , iron carbides and  $\text{Fe}_3\text{O}_4$  may be present during synthesis (3). Furthermore, the composition may change during synthesis (3). On the other hand, only iron carbide phases may form under other conditions of activation; a fraction of these iron carbide phases may undergo conversion to  $\text{Fe}_3\text{O}_4$  during synthesis (4).

In addition to the formation of iron carbide, excess carbon may be deposited during the activation procedure. The data from reference 5, plotted in Figure 1, provide an illustration of the relationship between the amount of excess carbon (free carbon, the carbon in excess of that liberated by dissolving iron carbide in acid). In this example, the extent of excess carbon was defined by controlling the activation temperature. The impact of the free carbon on the operation of the catalyst is defined, in this case, as the number of days that the catalyst exhibits greater than 80% CO conversion. The activity, based on this definition, exhibits a maximum in the region where the amount of free carbon is at its maximum value.

Huang et al. (4,6) found only  $\text{Fe}_3\text{O}_4$  by XRD analysis at the point of maximum activity. However, when syngas was utilized for pretreatment, only  $\text{Fe}_3\text{O}_4$  was detected and the catalyst exhibited low activity. Huang et al. (4,6) therefore assumed that an iron carbide phase must be present on the surface of an active catalyst and this surface phase is responsible for the catalytic activity.

The composition of the gases used during the pretreatment and/or reaction conditions with an iron catalyst can play a major role in the chemical composition and the phases of the compound present in the catalytic material (7). In some reactors, the catalyst may actually be present in several forms at any given time. For example, in a plug flow reactor the catalyst at the front (top) of the reactor is exposed to a reducing atmosphere whereas the catalyst at the back (bottom) of the reactor will experience an oxidizing atmosphere for operations at high conversion (8). Likewise, the gas composition and temperature of pretreatment may play an important role in the iron compounds that are present. For example, for a reduced catalyst, slight changes in the

H<sub>2</sub>/CO ratio and the temperature used for pretreatment can lead to either Häag carbide or cementite (Fe<sub>3</sub>C) (9).

Schroff et al. (10) have recently presented data for the activation of a precipitated iron oxide catalyst. These authors indicate that the activity correlates well with the extent of conversion of the iron oxide(s) into the carbide phase. They also report that an amorphous carbon film forms on the carbide particles during synthesis. Amorphous or even graphite-like phases of carbon may be present on small metal particles that have not been exposed to synthesis gas and/or conditions (11,12). Thus, a carbon overlayer appears to be a common feature of these metal carbide systems. The large iron oxide crystals that make up the catalyst utilized by Shroff et al. (10) indicate that it should not be considered as a typical high surface area precipitated iron oxide catalyst.

In the study by Shroff et al. (10) the assignment of the iron oxide/carbide phases depend upon lattice spacing measurements; this was true for both XRD and electron microscopic evidence. The lattice parameter data for several expected iron carbide phases and Fe<sub>3</sub>O<sub>4</sub> are given in Table 1. These lattice parameters were obtained from JCPDS (Joint Committee on Powder Diffraction Standards) powder diffraction files and these file numbers are also given in Table 1. In Figure 2, only the region of Fe<sub>3</sub>O<sub>4</sub> (400) profile is highlighted. The d-spacings for the (400) phase is 2.099 Å. The d-spacings given in reference (10) for magnetite and Fe<sub>x</sub>C phases are given in Table 2. The (400) planes of Fe<sub>3</sub>O<sub>4</sub> (magnetite) are separated by 2.099 Å. The percent error in the observation of Fe<sub>3</sub>O<sub>4</sub> (311) planes (Table 2), varies from -5.2% to +0.434%. Applying a nominal ± 5% error to the measurements for the (400) planes of Fe<sub>3</sub>O<sub>4</sub> would place it in the range of 1.994-2.204 Å, also shown in Figure 2. Hence, the observation of 2.0, 2.2,

2.05 or 2.17 Å lattices might equally as well been assigned to  $\text{Fe}_3\text{O}_4$  as to the carbide phases. While the 2.1 Å region was used for this illustration, similar considerations apply for most other regions of possible lattice spacings.

Furthermore, it was claimed that the  $\text{Fe}_3\text{O}_4$  [400] planes are overlapped by the peaks of carbides in XRD patterns (Figures 4, 5 and 6 in reference 10). In Figure 2, it can be seen that the  $\Delta d$  between the  $\text{Fe}_3\text{O}_4$  [400] planes and the  $\epsilon'$ - $\text{Fe}_{2.2}\text{C}$  [101] planes is only 0.037 Å. Assignment of  $\text{Fe}_x\text{C}$  phases to the planes reported in reference 10 with d-spacings that are so similar must be viewed with caution.

In the present investigation, the  $\text{Fe}_2\text{O}_3$  catalyst consisted of ultrafine particles ( $\leq 3$  nm; 300  $\text{m}^2/\text{g}$  surface area). Samples of the catalyst were withdrawn at intervals during activation and the initial synthesis period. The structural characterization was carried out using electron microdiffraction technique, since this technique is suitable for obtaining structural information from small individual particles. Furthermore, the  $\text{Fe}_3\text{O}_4$  and iron carbide phases can be distinguished using this technique because of the different crystal structures of these materials (Table 1).

## EXPERIMENTAL METHODS

Two grams of  $\text{Fe}_2\text{O}_3$  (Mach, Inc.) were loaded into a continuous stirred tank reactor (CSTR) using tetralin as the solvent. Then carbon monoxide at 100 psig was passed through the reactor which was heated to 260°C during one hour and was held at 260°C for the remainder of 24 hours. A mixture of  $\text{CO}/\text{H}_2 = 1$  at 100 psig was then passed through the reactor and slurry samples were withdrawn through a tube that extended below the liquid level at 2, 10, 24, 36, 48 and 72 hours of exposure to  $\text{CO}/\text{H}_2$  synthesis gas. Thus, the hours given refer to the length of time the sample was exposed to synthesis gas following a 24 hour pretreatment with CO.

Preparation of a sample for TEM analysis involved adding a few drops of the suspension of catalyst in tetralin plus reactor wax to ethanol and then placing the sample in an ultrasonic bath to develop a fine dispersion. A drop of the final suspension was placed on a carbon coated 200 mesh copper grid. After the ethanol evaporated, a thin layer of particles remained on the carbon film that is suitable for examination in the electron microscope.

Prior to the introduction of the Scanning Transmission Electron Microscope (STEM) technique, the lens configuration used for diffraction studies was limited by the spherical aberration of the objective lens, and this allows diffraction patterns to be obtained only from regions larger than 500nm. This limitation can be bypassed by means of microdiffraction, which has the advantage of forming diffraction patterns from regions as small as 2nm. Microdiffraction provides the means to reduce the total diffraction-forming volume and, in turn, increases the contribution from the very small regions (as small as 2nm) of interest. The result is a diffraction pattern with an improved signal-to-noise ratio. The instrument used for this study provides means to obtain diffraction patterns from regions of 2nm, 5nm and 10nm in diameter. Thus, this technique is especially suitable for obtaining diffraction patterns from individual particles of these sizes.

TEM examination was performed using a Hitachi H800 NA microscope at an operating voltage of 200 kV. Microdiffraction and EDX analysis were carried out in the nanoprobe mode, using an incident beam of 2 nm or 5 nm in diameter. This microscope is equipped with a silicon-lithium diode X-ray detector (Link Analytical Limited) and a multi-channel analyzer (Tracor 500). The X-rays emitted from the

specimen upon electron irradiation were collected in the range 0.1 - 20 keV for 60 seconds.

## RESULTS

The vendor identified the as-received sample as  $\gamma\text{-Fe}_2\text{O}_3$  based on electron diffraction pattern. A typical electron micrograph from this as-received powder is shown in Figure 3. The electron microdiffraction pattern, obtained from a 5 nm region, in the inset of Figure 3 exhibits only two diffuse rings.  $\gamma\text{-Fe}_2\text{O}_3$  has a simple cubic structure; hence, reflections from all the planes are possible. The distance from the center to the rings or to the diffraction spots is indicative of the lattice spacing of particular [hkl] planes. Diffraction rings appear for polycrystalline materials as well but these would be sharp and distinct with the continuous array of reciprocal-lattice points which are concentric spheres in reciprocal space indicating random orientation. However, these rings will be diffuse and not sharp for amorphous materials where a lack of crystal structure is evident, or for materials containing nanosized ultrafine particles. The diffuseness and variations in intensity profiles result from inelastic scattering phenomena.

The ratio of the distances,  $d$ , from the center to the midpoint of each of the two consecutive rings in Figure 3 is 1.625. This could correspond to  $d_1/d_2 = 2.52/1.55 = 1.6258$  as  $d_{311} = 2.52 \text{ \AA}$  and  $d_{520} = 1.55 \text{ \AA}$ . This indicates that the first diffuse ring could be due to the [311] planes of the simple cubic structure of  $\gamma\text{-Fe}_2\text{O}_3$ , while the second ring would be due to the [520] planes. The intensity calculations show that the [311] planes have the highest intensity while the [520] planes have intensity  $< 1\%$  relative to the [311] plane. Hence, it is unlikely that the second ring is from the [520] planes. Therefore, based on this electron microdiffraction pattern, we believe that this ultrafine

material may be considered to be amorphous as far as either electron or X-ray diffraction is concerned.

An electron micrograph was obtained for the two hour sample and the particle size distribution histograms obtained from measuring hundreds of particles of each of the catalyst samples are shown in Figure 4. It can be discerned that the major fraction of particles for the 2 hour sample are in the neighborhood of 5 nm in size. As the particles were extremely small, an electron probe of 2nm in diameter was used for obtaining microdiffraction patterns. A typical microdiffraction pattern obtained from an individual particle shows that this particle is body centered orthorhombic  $\text{Fe}_3\text{C}$  phase which is oriented in the [110] direction with respect to the incident beam. The microdiffraction pattern shows that this particle is body centered orthorhombic  $\text{Fe}_3\text{C}$  phase which is oriented in the [110] direction with respect to the incident beam. Microdiffraction patterns obtained from other particles also exhibited patterns for the  $\text{Fe}_3\text{C}$  phase. However, these fine particles consist of a very limited number of planes which results in a limited number of diffraction spots in the diffraction pattern.

For each sample, the sizes of 100-200 particles from different regions of the samples were measured and the particle size distributions for each sample are given in Figure 5. The major fraction of the particle size distributions (peak distribution) are plotted against time in Figure 6 and the particle sizes appear to follow an S-shape growth pattern; however, this conclusion of an S-shaped pattern is based only on the size of the 72 hour sample. If the 72 hour sample is ignored, the growth is then one of a rapid initial growth followed by a period of constant particle size. The limited amount of catalyst that could be handled in the reactor limited the number of samples that could

be collected during the experiment; hence, more data would be required to decide which growth pattern is followed.

A bright field image was obtained from the ten hour sample and two types of particles can be seen for this sample (Figure 7). One kind of particles appears transparent (lighter) and another kind appears to be black and dense. Tilting the specimen by about  $4^\circ$ , did not change or modify the image of the light and dark particles. Even after tilting the specimen, the light and dark particles retained the same shape and contrast. Hence, attempts were made to distinguish between these two types of particles using the microdiffraction technique. Several microdiffraction patterns using a 5 nm probe were obtained from both types of particles in this sample. As the particles are larger, a greater number of diffraction spots were obtained than was the case for the 2 hour sample. The diffraction patterns obtained from the dark, dense particles show that these particles are carbide phases ( $\text{Fe}_3\text{C}$  or  $\text{Fe}_{2.2}\text{C}$ ). A typical microdiffraction pattern obtained from a dark particle of  $\text{Fe}_3\text{C}$  is presented in Figure 8(a). On the other hand, the lighter particles exhibit the pattern expected for the  $\text{Fe}_3\text{O}_4$  phase (magnetite); a typical microdiffraction pattern obtained from a single transparent particle is presented in Figure 8(b). Also a few dark particles exhibit the  $\text{Fe}_{2.2}\text{C}$  phase; a typical microdiffraction pattern from one of these particles is presented in Figure 8(c). Microdiffraction patterns obtained from about 25-30 particles consistently showed that the dark particles were a crystalline iron carbide phase and the light particles were of the  $\text{Fe}_3\text{O}_4$  phase.

The iron carbides have different phases with corresponding lattice parameters from those of  $\text{Fe}_3\text{O}_4$  and these are tabulated in Table 1. In the X-ray diffraction patterns, the (400) profile of  $\text{Fe}_3\text{O}_4$  is overlapped by one profile of  $\epsilon\text{-Fe}_{2.2}\text{C}$  (see Figure

9). The d-spacings of  $\text{Fe}_3\text{O}_4$  and other carbide phases are illustrated in Figure 2. The difference in d-spacings between  $\text{Fe}_3\text{O}_4$  and iron carbides can be easily distinguished by microdiffraction because this difference causes different locations for the diffraction spots, other conditions such as camera length remaining the same. For example, the diffraction spots in  $\{110\}$  diffraction pattern of  $\text{Fe}_3\text{O}_4$  will be located differently from those of  $\text{Fe}_{2.2}\text{C}$   $\{100\}$  pattern. Solving these diffraction patterns will clearly indicate the phase of particle and the orientation. In this way, all the diffraction patterns were solved and the results showed consistently that the dark/dense particles are iron carbide and light particles are  $\text{Fe}_3\text{O}_4$ .

Two factors influence the location of the diffraction spots such as shown in figure 8a-c: the crystal structure and the lattice spacing of the particular plane that is oriented to the electron beam to satisfy the Bragg diffraction condition.  $\text{Fe}_3\text{O}_4$  has a cubic structure whereas the iron carbide structures of interest are either monoclinic or orthorhombic. The number and spatial arrangement of the diffraction spots about the central electron beam will be uniquely determined by the crystal structure. Thus, since  $\text{Fe}_3\text{O}_4$  has a cubic structure the diffraction spots will appear in a geometric arrangement that uniquely identifies this phase and thereby eliminates from consideration the iron carbide phases given in Table 1. This is not the case for the iron carbide phases since two or more phases have the same crystal structure (Table 1). Thus, the identification of an iron carbide phase depends upon matching the distance of the spots from the spot representing the incoming electron beam and, since this will depend upon the lattice spacing, this identification suffers the same deficiency as the identification of crystal phase by X-ray diffraction. thus, the identification of the  $\text{Fe}_3\text{C}$  and  $\text{Fe}_{2.2}\text{C}$  in

Figure 8 is not unique but represents a fitting of theory and the diffraction spots that is consistent with the crystal structure and the diffracting plane given in Figure 8.

A micrograph obtained from the 48-hour sample again showed two kinds of particle morphology. Microdiffraction patterns obtained from the darker particles using a 5 nm electron probe identified iron carbide phases, whereas the lighter particles exhibited  $\text{Fe}_3\text{O}_4$  phase.

A typical micrograph obtained from the 72-hour sample shows that the particles have grown to about 30 nm in size during 72 hours of syngas conversion, and many particles exhibit a "core/shell" structure (Figure 10). Using a 5 nm probe, electron diffraction patterns were obtained from the core, which exhibited patterns characteristic of iron carbide phases. A typical microdiffraction pattern obtained from the core of a particle is presented in Figure 11 and it exhibits a typical pattern for  $\text{Fe}_3\text{C}$  in [111] orientation. Electron microdiffraction patterns could not be obtained from the region that comprise the shell. Microdiffraction patterns obtained from the less dense transparent particles showed the  $\text{Fe}_3\text{O}_4$  phase.

The population of light and dark particles are plotted in Figure 12 for the 24 and 72 hour samples. Whereas the carbide particles (i.e., dark/dense particles) are more prevalent in the 24 hour sample, the oxide particles (i.e., light particles) are more prevalent in the 72 hour sample. It appears that the water and/or carbon dioxide produced during the FT synthesis causes oxidation of the carbide which results in the formation of iron oxide. A typical particle size histogram is presented in Figure 13 for the 24 hour sample; this shows the surprising result that there is no significant difference in size distribution between the carbide and oxide particles.

## DISCUSSION

The present data, combined with those obtained by Huang et al. (4,6), show that a large fraction (0.8 or greater) of the ultrafine iron oxide is converted to iron carbide ( $\text{Fe}_3\text{C}$ ) following 24 hours of pretreatment in CO at 260°C. However, this carbide is not stable under synthesis conditions and a large fraction of it is gradually transformed to an iron oxide ( $\text{Fe}_3\text{O}_4$ ).

The data of the current study ( $\blacktriangle$ ) show less  $\text{Fe}_3\text{O}_4$  than was obtained for the same time of exposure to syngas during the earlier study using Mössbauer data to identify iron compounds (Figure 14;  $\blacksquare$ ), reference 4). Thus, different methods were used to obtain the percentage of  $\text{Fe}_3\text{O}_4$  in these two studies. In fact, it is gratifying that the TEM data ( $\blacktriangle$ ), which identifies only the fraction of iron in particles large enough to visually identify, agrees so well with the compositions obtained from Mössbauer data, which identifies all of the iron present in the sample.

There is a significant increase of the average particle size during carbiding by CO during 24 hours at 260°C. Following introduction of the synthesis gas there is a period of about 20 hours where particle growth occurs with nearly a 10-fold increase in the particle diameter (1,000-fold volume increase). This volume increase obtained from TEM data corresponds to a significant decrease in the geometrical surface area of the catalyst from about 300  $\text{m}^2/\text{g}$  to about 30  $\text{m}^2/\text{g}$ , and this decrease is verified by the surface areas obtained from the BET method.

A comparison of the data in Figure 13 for the oxide (lighter) and carbide (darker) particles show that the two forms have essentially the same size distribution. This is surprising since the oxide form was not present in a significant amount following activation (0 hour sample), and must therefore be formed from the carbide particles.

This could be the result of a very dynamic system in which a particle undergoes transformations between the carbide and oxide forms. It could also result from a gradual growth of the carbide particles and their subsequent irreversible oxidation to  $\text{Fe}_3\text{O}_4$ . The data do not permit a distinction between these two possibilities or other possibilities.

It is realized that the appearance of the lighter and darker particles could be caused by variations in diffraction contrast between otherwise identical particles. If diffraction contrast is responsible for this appearance, particles will "twinkle" between lighter and darker spots when they are tilted in and out of strong diffraction conditions. However, it seems unlikely that two samples (samples after 10 and 48 hours of synthesis) would have orientations so that one sample has about two times as many of the darker, and half as much of the lighter, particles than the other sample. Furthermore, the same trend for the oxide fraction was obtained from the TEM and the Mössbauer data and this adds credence to the assignment of the lighter and darker particles to oxide and carbide form, respectively. Likewise, it is preferred to obtain the crystal symmetry and unit cell measurements from patterns that are taken close to the major zone axes. This is a concern but, since several, if not all, of the microdiffraction patterns were obtained for the preferred orientation we should have obtained both iron oxide and iron carbide patterns for the lighter and the darker particle groupings. In contrast, this was not the case. In spite of these limitations, the observation that the lighter and darker particles have a similar size distribution requires the iron oxide and iron carbide particles to have the same size distribution. This is an important observation because it indicates that there is not a preferred size for these two iron

compounds and that the iron carbide particle transforms to a similar sized iron oxide particle.

Following a period of synthesis, particles with a solid core surrounded by a shell of less dense materials were observed. One could assign the composition of these particles by analogy with the results reported by Shroff et al. (10); that is, the core would be an iron carbide and the shell could be a carbon overlayer. This observation may also be due to sample preparation for the TEM measurements. One could assume that the suspension contained both small (submicron) and larger (in the 5-30 nm) particles. As the solvent evaporates, the larger particles will retain solvent; thus, these solid particles can be viewed as being surrounded by a solvent "drop" that contains many smaller particles. The final evaporation would deposit a ring of these small particles around the larger particles. This latter view is, in a sense, analogous to the ring of dust particles that are formed when water drops evaporate on a wax surface.

The 24-hour CO pretreatment results in the formation of about two times as much carbon dioxide as would be needed to form  $\text{Fe}_{2.2}\text{C}$ ; thus, it appears that the 24-hour CO activation must deposit "free carbon" on and/or in the iron carbide particles. However, since hydrogen is not present during the 24-hour activation, this carbon cannot be present as some adsorbed hydrocarbon material.

The TEM examination combined with microdiffraction provides a valuable technique for characterization of Fischer-Tropsch catalysts. Under suitable conditions a reasonable quantitative estimation of crystal phases can be determined, as in the present study.

## **ACKNOWLEDGMENT**

Financial support for this work was provided by the U.S. DOE through contract number (DE-AC22-91PC90056) and the Commonwealth of Kentucky.

## REFERENCES

1. R. B. Anderson, "The Fischer-Tropsch Synthesis", Academic Press, New York, NY, 1984.
2. H. H. Storch, N. Golombic and R. B. Anderson, "The Fischer-Tropsch and Related Synthesis," John Wiley & Sons, Inc., New York, 1951.
3. H. Pichler and A. Hector in "Kirk-Othmer Encyclopedia of Chemical Technology," Wiley, New York, Vol. 4, 2nd Edition, (1963), pp 446-489; reproduced from O. G. Malan, J. D. Louw and L. C. Ferreira, *Brenstoff-Chem.*, **42**, 209 (1961).
4. C. S. Huang, B. Ganguly, G. P. Huffman, F. Huggins B. H. and Davis, *Fuel Sci. Tech. Int.*, 11, 1289 (1993).
5. L. J. E. Hofer, E. M. Cohn and W. C. Pebbles, *J. Am. Chem. Soc.*, **71**, 189 (1949).
6. C. S. Huang, L. Xu and B. H. Davis, *Fuel Sci. Tech. Int.*, **11**, 639 (1993).
7. B. H. Davis, "Final Technical Report. Technology for Iron Fischer-Tropsch Catalysts," Contract #DE-AC22-91)C90056, 1995.
8. M. D. Dry, in "Applied Industrial Catalysis," **2**, 1983, 167.
9. R. B. Anderson, "The Fischer-Tropsch Synthesis", Academic Press, New York, NY, 1984, pp 30-31.
10. M. D. Shroff, D. S. Kalakkard, K. E. Coulter, S. D. Köhler, M. S. Harrington, N. B. Jackson, A. G. Sault and A. K. Dayte, *J. Catal.*, **156**, 185 (1995).
11. P. E. Nolar, D. C. Lynch and A. H. Cutler, *Carbon*, **32**, 477 (1994).
12. R. Ochoa, X. X. Bi, A. M. Rao and P. C. Eklund in "Transition Metal Nitride and Carbide Nanoparticles," (S. T. Oyama, Ed.), Blackie Academic & Professional, London, 1996.

Table 1					
Lattice Parameter Data for Different Iron Carbides					
			Lattice Parameters (Å)		
Name	Structure	PDF Card #	a	b	c
Fe <sub>3</sub> O <sub>4</sub>	Cubic	19-629	8.396		
χ-Fe <sub>2.5</sub> C	Monoclinic	36-1248	11.563	4.573	5.058
ε-Fe <sub>2</sub> C	Orthorhombic	26-782	4.704	4.295	2.830
ε <sup>1</sup> -Fe <sub>2.2</sub> C	Monoclinic	17-897	2.794	2.794	4.360
Fe <sub>3</sub> C	Orthorhombic	35-772	5.0910	6.7434	4.526
FeC	Orthorhombic	3-411	4.30	2.50	6.70

Table 2					
Lattice Spacings (Å)		Phase	Planes	Fig. # in Ref. 10	% Error
True Value	Observed in Ref. 10				
3.684	3.7	$\alpha\text{-Fe}_2\text{O}_3$	[012]	13	+ 0.434
2.532	2.4	$\text{Fe}_3\text{O}_4$	[311]	14(a)	- 5.2
2.532	2.4	$\text{Fe}_3\text{O}_4$	[311]	14(c)	- 5.2
2.532	2.5	$\text{Fe}_3\text{O}_4$	[311]	14(d)	- 1.26
2.532	2.450	$\text{Fe}_3\text{O}_4$	[311]	15(a)	- 3.239
2.532	2.50	$\text{Fe}_3\text{O}_4$	[311]	15(b)	- 1.26
2.532	2.4	$\text{Fe}_3\text{O}_4$	[311]	15(c)	- 5.2
2.532	2.46	$\text{Fe}_3\text{O}_4$	[311]	16(a)	- 2.84
2.532	2.4	$\text{Fe}_3\text{O}_4$	[311]	16(b)	- 5.2
2.532	2.5	$\text{Fe}_3\text{O}_4$	[311]	16(c)	- 1.26
	2.2	$\text{Fe}_x\text{C}$		14(c)	
	2.01	$\text{Fe}_x\text{C}$		15(a)	
	2.0	$\text{Fe}_x\text{C}$		15(a)	
	2.05	$\text{Fe}_x\text{C}$		15(b)	
	2.0	$\text{Fe}_x\text{C}$		15(c)	
	2.17	$\text{Fe}_x\text{C}$		16(a)	
	2.10	$\text{Fe}_x\text{C}$		16(b)	
	2.0	$\text{Fe}_x\text{C}$		16(c)	

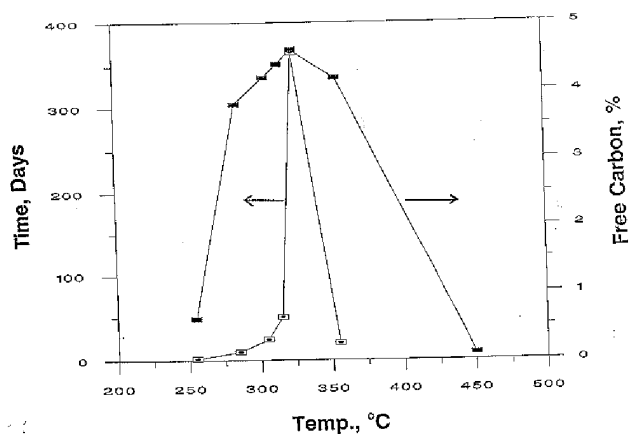


Figure 1. Dependence of the "free carbon" (see text for definition) and the catalyst activity/stability upon the activation temperature (plot of data from reference 5).

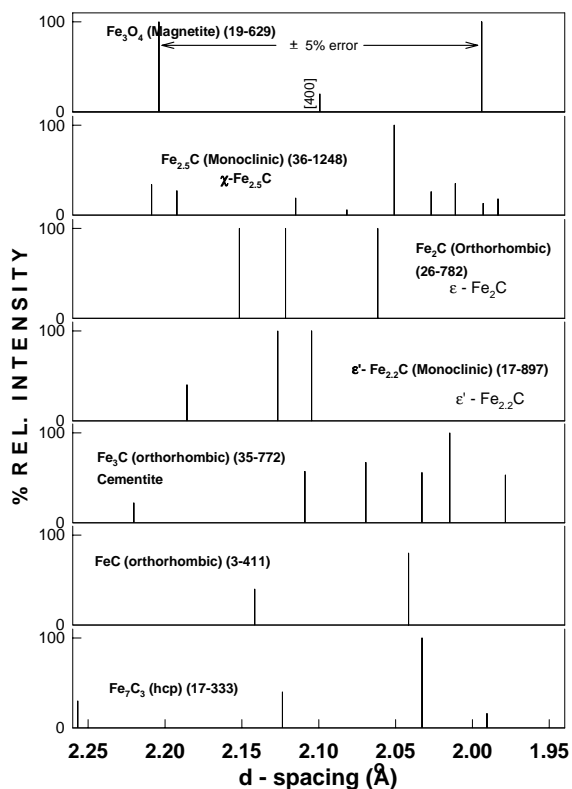


Figure 2. Region of the d-spacing that contains the most intensive peak(s) for various d-spacing for iron carbide phases compared to position  $\pm 5\%$  for error for the [400] line for  $\text{Fe}_3\text{O}_4$ .

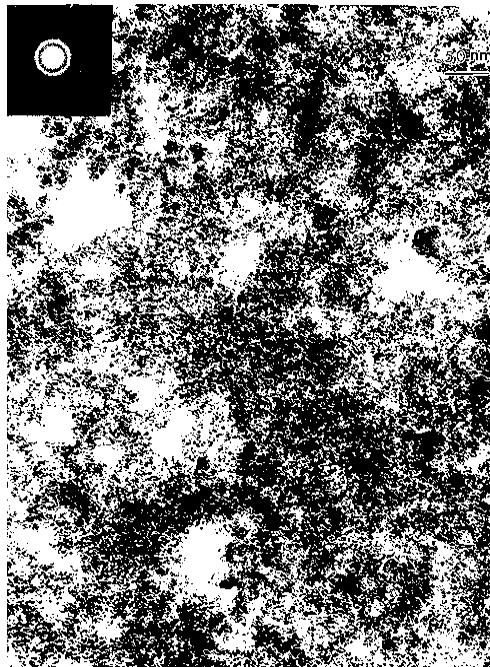


Figure 3. A TEM picture of ultrafine  $\text{Fe}_2\text{O}_3$  particles of  $\leq 3$  nm. The inset is the microdiffraction pattern obtained from an aggregate using a 2 nm electron probe, which shows diffuse rings.



Figure 4. Electron micrograph showing a uniform distribution of particles for the 2 hr. sample.

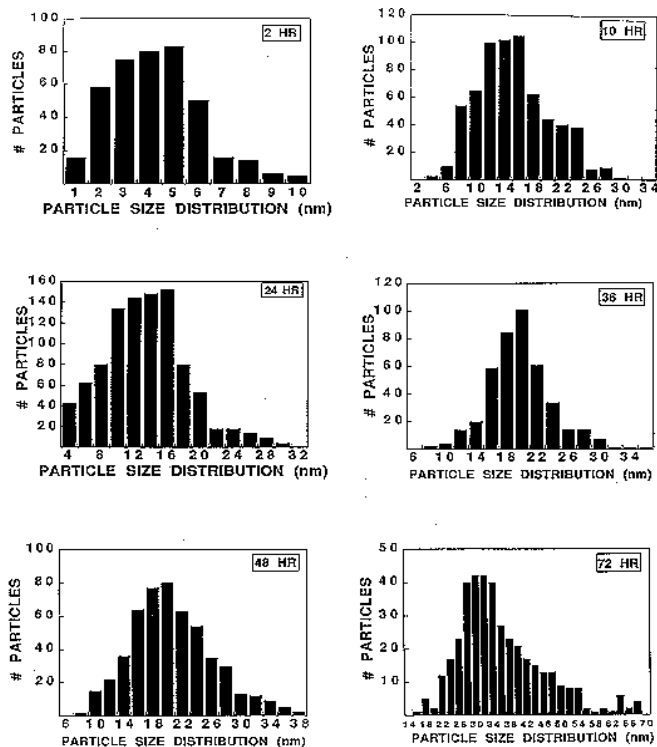


Figure 5. Particle size distribution histogram obtained from TEM for catalysts withdrawn at increasing synthesis times.

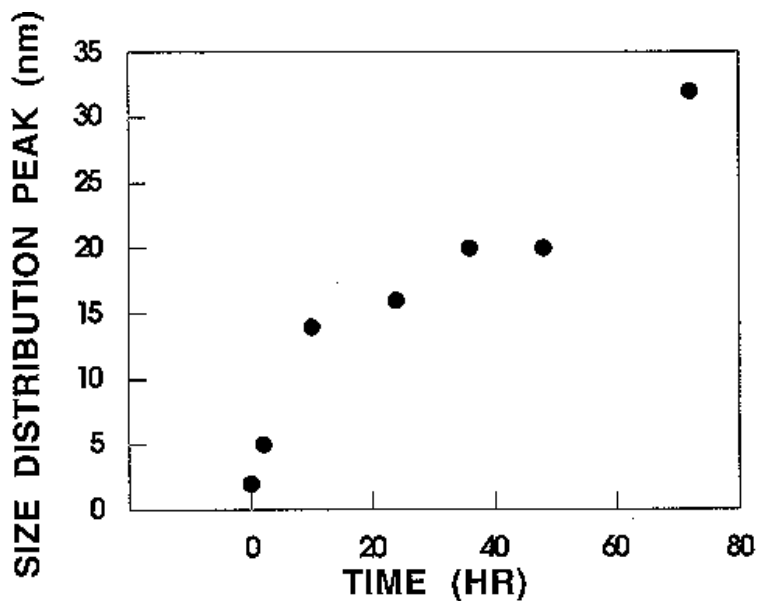


Figure 6. Average particle size versus time in the reactor.

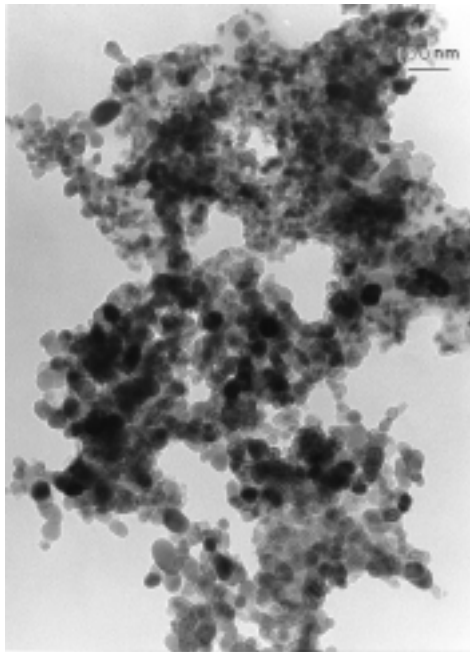


Figure 7. A bright field image obtained from the 10 hr. sample.

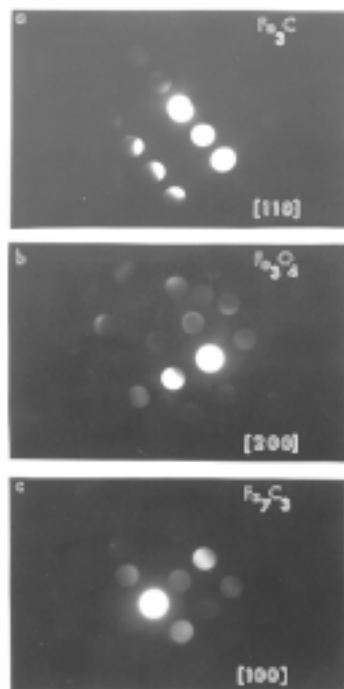


Figure 8. Electron microdiffraction patterns using a 5 nm electron beam from the 10 hour sample. (a) pattern from a dark/dense particle, showing  $\text{Fe}_3\text{C}$  particle in  $[110]$  orientation. (b) pattern from a lighter particle, showing  $\text{Fe}_3\text{O}_4$  phase in  $[100]_{\text{fcc}}$  orientation, and (c) pattern from another dark/dense particle showing  $\text{Fe}_{2.2}\text{C}$  phase oriented in  $[100]$  direction.

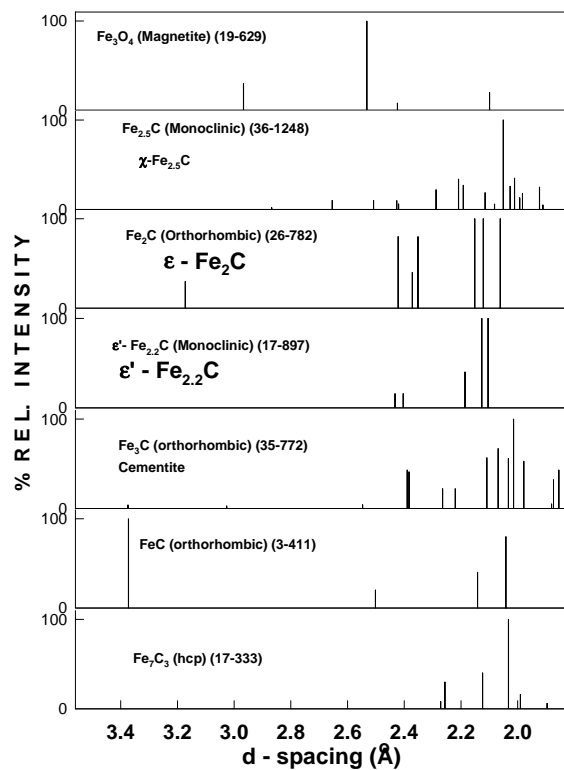


Figure 9. Relative intensity for XRD peaks for  $\text{Fe}_3\text{O}_4$  and iron carbides for a range of d-spacings.

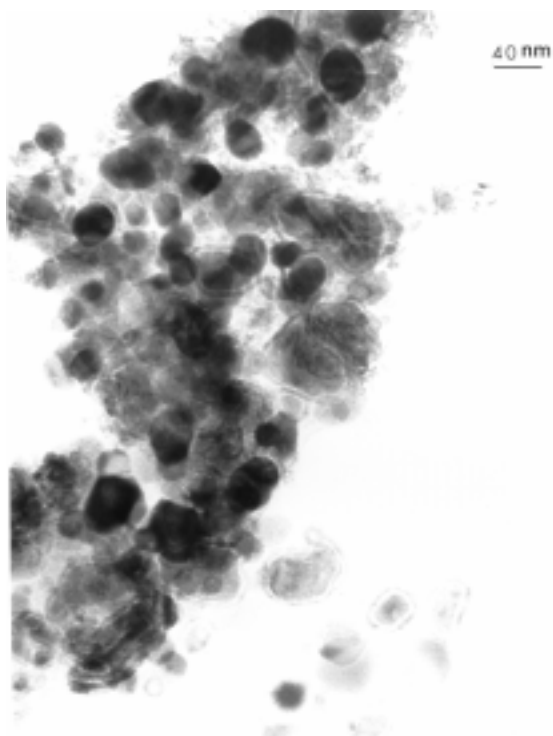


Figure 10. An electron micrograph from 72 hr sample depicting the core/shell type morphology.

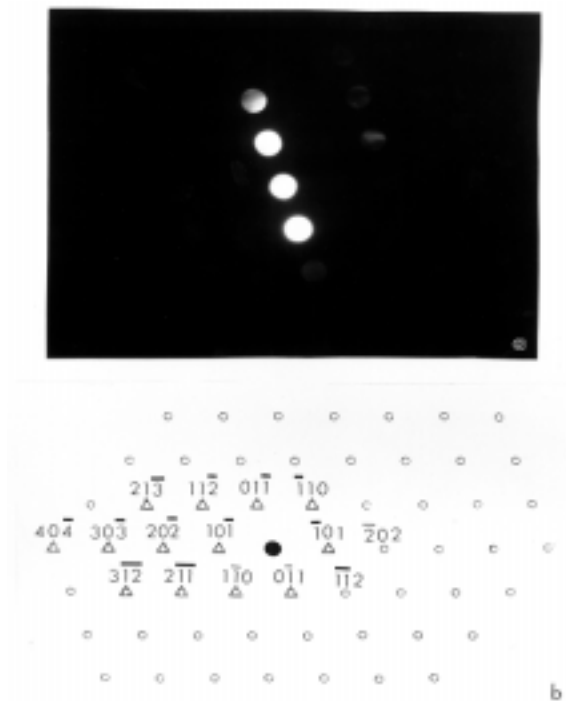


Figure 11. Electron microdiffraction pattern obtained from the core showing  $\text{Fe}_3\text{C}$  phase in  $[111]$  orientation. (a) Experimentally obtained pattern, and (b) (○) theoretically generated reflections for  $[111]$  orientation of  $\text{Fe}_3\text{C}$  phase and (Δ) experimentally obtained reflections.

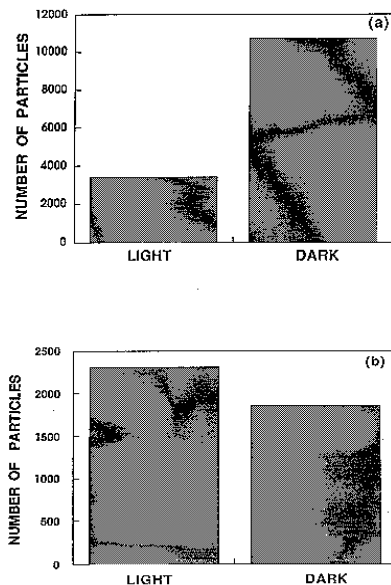


Figure 12. The average population of light and dark particles for the (a) 24 hr. sample and (b) 72 hr. sample.

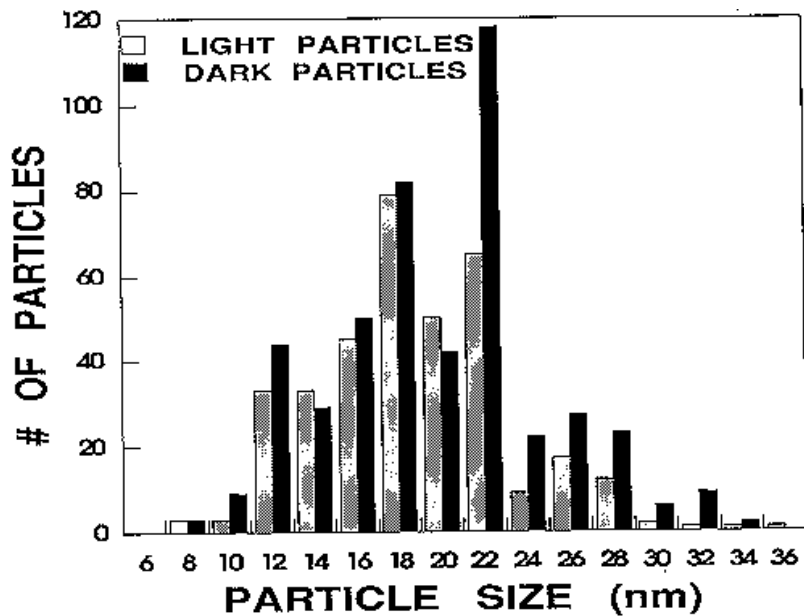


Figure 13. Particle size distribution for light and dark particles for the 24 hr. sample.

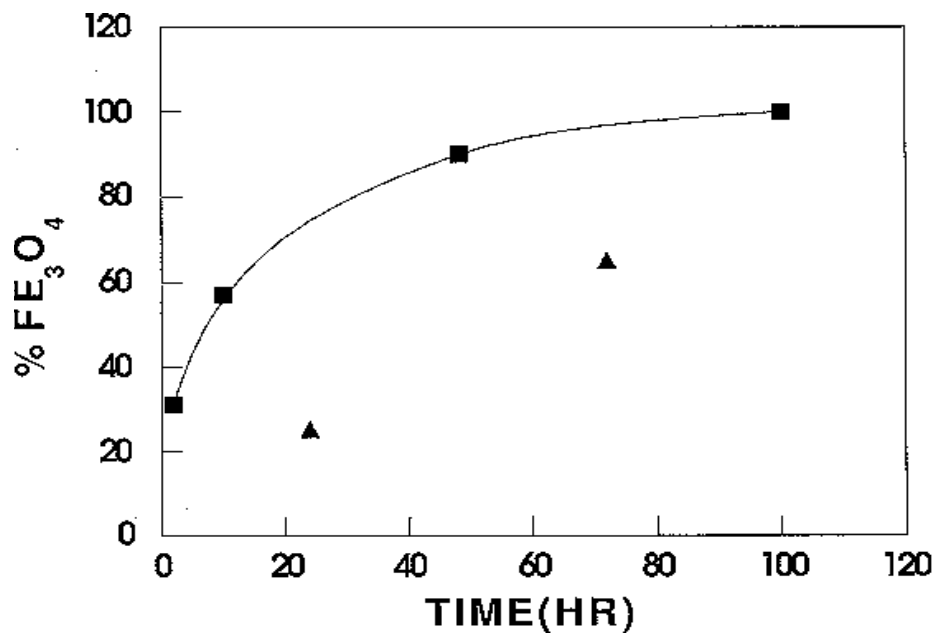


Figure 14. Comparison of the percentage of iron oxide from Figure 11 (▲) with the percentage of iron oxide reported by Huang et al. (8) for Mössbauer data from a similar study (■).